Quantum wave packet *ab initio* molecular dynamics: An approach to study quantum dynamics in large systems

Srinivasan S. Iyengar[a] and Jacek Jakowski
Department of Chemistry and Department of Physics, Indiana University, Bloomington, Indiana 47405

(Received 2 December 2004; accepted 24 January 2005; published online 21 March 2005)

A methodology to efficiently conduct simultaneous dynamics of electrons and nuclei is presented. The approach involves quantum wave packet dynamics using an accurate banded, sparse and Toeplitz representation for the discrete free propagator, in conjunction with *ab initio* molecular dynamics treatment of the electronic and classical nuclear degree of freedom. The latter may be achieved either by using atom-centered density-matrix propagation or by using Born–Oppenheimer dynamics. The two components of the methodology, namely, quantum dynamics and *ab initio* molecular dynamics, are harnessed together using a time-dependent self-consistent field-like coupling procedure. The quantum wave packet dynamics is made computationally robust by using adaptive grids to achieve optimized sampling. One notable feature of the approach is that important quantum dynamical effects including zero-point effects, tunneling, as well as over-barrier reflections are treated accurately. The electronic degrees of freedom are simultaneously handled at accurate levels of density functional theory, including hybrid or gradient corrected approximations. Benchmark calculations are provided for proton transfer systems and the dynamics results are compared with exact calculations to determine the accuracy of the approach. © *2005 American Institute of Physics*. [DOI: 10.1063/1.1871876]

I. INTRODUCTION

The time-dependent Schrödinger equation is the starting point for a number of computational methods in gas-phase[1] and condensed phase quantum dynamics.[2] In many cases the Born–Oppenheimer approximation is invoked which allows for propagation of nuclei, quantum-mechanically,[1,3–29] classically,[30–34] or semiclassically,[35–42] on fitted electronic surfaces. These potential energy surfaces may be either obtained from highly accurate, but demanding, electronic structure calculations or from parametrizations of the associated electronic surfaces. In the former case, the required number of quantum chemical calculations can be very large depending upon the size of the system. It is in this regard that "on-the-fly" approaches to dynamics of nuclei and electrons[30–35,43–45] have recently become popular, leading to the field of *ab initio* molecular dynamics.[46] Here, an approximation to the electronic wave function is propagated along with the nuclear degrees of freedom to simulate dynamics on the Born–Oppenheimer surface. If the nuclei are treated classically[32–34,43,44,47] then the forces on the nuclei are determined from the electronic structure. This approach, when combined with full quantum or semiclassical dynamics schemes, has the potential to treat large problems accurately with the complete machinery of quantum dynamics. Several steps have been taken in this direction.[48–50]

In the current paper, a new approach is proposed that attempts to overcome some bottlenecks in this area. The method discussed here combines full quantum wave packet dynamics treatment of the time-dependent Schrödinger equation with *ab initio* molecular dynamics. The latter is performed using atom-centered density-matrix propagation (ADMP)[34,51] and Born–Oppenheimer molecular dynamics.[30,31,33] The wave packet dynamics is performed through an analytic, banded, Toeplitz[52] approximation to the discretized free propagator.[29,53–57] Some features of this approach include: (a) accurate treatment of the electronic degrees of freedom by including hybrid density functionals (e.g., B3LYP), (b) formally exact and efficient quantum propagation where the numerical description of the wave packet adapts to the shape and position of the same to provide a flexible propagation scheme, (c) efficient treatment of large systems based on established linear scaling electronic structure techniques.[58–60] The current work, thus, attempts an important synergy between formally accurate approaches in quantum scattering theory[1,5,6,9,10,12,26,38–40,55,61,62] and approximate *ab initio* molecular dynamics methods[30–34,43,45,51,63–67] to achieve efficient quantum dynamics of large systems.

Our approach differs from other efficient quantum dynamics methodologies that propagate the Feynman path centroid[49,50] in allowing accurate treatment of the electronic structure through the use of hybrid density functionals such as B3LYP. Another important difference is based on the fact that the delocalization of a quantum particle may change during dynamics on a corrugated surface and this is accounted for in the current scheme by use of an adaptive grid description of the wave packet. This is in contrast to standard implementations of the Feynman path centroid scheme where a fixed number of Feynman path discretizations (or beads) are retained throughout the dynamics process.[49,50]

The paper is organized as follows: In Sec. II we con-

[a]Electronic mail: iyengar@indiana.edu

struct the theoretical formalism. This leads to a discussion of quantum wave packet dynamics in Sec. II A and the ADMP approach to dynamics of electrons and classical nuclei in Sec. II B. Some computational aspects of the methodology are discussed in Sec. II C. Section III deals with a discussion of the numerical tests and results. This is done in three parts: In Sec. III A the accuracy and efficiency of the wave packet dynamics algorithm is evaluated. Its synergy with *ab initio* ADMP and Born–Oppenheimer dynamics is tested and compared as part of Sec. III B. In Sec. III C we present an application to a larger problem to demonstrate the potential of the approach in studying important chemical problems. The chosen application in Sec. III C is one that has been considered prototypical[40] in condensed phase proton transfer as well as in weak acid-base chemistry.[68] In Sec. IV we present our conclusions.

II. WAVE PACKET GENERALIZATION FOR THE ATOM-CENTERED DENSITY-MATRIX PROPAGATION (ADMP) AND BORN–OPPENHEIMER DYNAMICS SCHEMES

To derive wave packet generalizations, we start with the full time-dependent Schrödinger equation:

$$\iota\hbar\frac{\partial}{\partial t}\psi(r,R;t)=\mathcal{H}\psi(r,R;t), \tag{1}$$

where $\mathcal{H}$ is the full electron nuclear Hamiltonian and $\psi(r,R;t)$ is the state vector that describes the electron-nuclear system at time t. To proceed further we recognize that in large systems, some nuclei in the system may require only classical treatment. But other parts of the system (such as electrons or nuclei with relatively large de Broglie wavelengths) may need to be treated by applying full quantum dynamics or an approximation to the same. If we assume that these individual parts of the full system only interact with each other in an average sense then we may employ a time-dependent self-consistent field (TDSCF)-like[69–71] partitioning scheme where the full electron-nuclear system is divided into three parts: The first portion comprises a subsystem that will eventually be treated using quantum dynamics and the position variables for the particles in this part are denoted by R_{QM}, the second subsystem comprises most of the nuclear degrees of freedom and will eventually be treated within a classical framework (note that some nuclei may be included in the first part treated with quantum dynamics) and the position variables for these particles are denoted by $\mathbf{R_C}$ in the following discussion, and the third portion comprises the electrons in the system. Based on the time-dependent self-consistent field technique[69–72] we can now reduce Eq. (1) into three separate equations one describing each subsystem:

$$\iota\hbar\frac{\partial}{\partial t}\psi_1(R_{\mathrm{QM}};t)=\mathcal{H}_1\psi_1(R_{\mathrm{QM}};t), \tag{2}$$

$$\iota\hbar\frac{\partial}{\partial t}\psi_2(\mathbf{R_C};t)=\mathcal{H}_2\psi_2(\mathbf{R_C};t), \tag{3}$$

$$\iota\hbar\frac{\partial}{\partial t}\psi_3(r;t)=\mathcal{H}_3\psi_3(r;t), \tag{4}$$

where $\mathcal{H}_1$ is the average (or effective) Hamiltonian of system 1 and is written as $\langle\psi_2\psi_3|\mathcal{H}|\psi_2\psi_3\rangle$. $\mathcal{H}_2$ and $\mathcal{H}_3$ are defined similarly. It must be noted that Eqs. (2)–(4) are obtained by writing the full wave function $\psi(r,R;t)\equiv\psi_1\psi_2\psi_3\exp[\iota\gamma]$ where $d\gamma/dt$ is proportional to twice the energy of the system. System 1 is to be treated quantum-dynamically. Since system 2 comprises nuclei that are not required to be treated within a quantum dynamical formalism (since they are not part of system 1), we enforce the classical limit ($\hbar\to 0$) for these particles to obtain a classical Hamilton–Jacobi equation[65,73–81] to describe this portion of the system. In system 3, which comprises electrons, we choose to enforce the space–time separation to obtain a stationary state description of electrons. In this fashion one recovers a formalism where a portion of the full system is treated using quantum dynamics, another portion of the system is treated classically, while a third portion (the electrons) is described within a stationary state approximation. In absence of system 2, the partitioning scheme reduces to the adiabatic approximation of electrons and nuclei which has been the cornerstone for many time-dependent as well as time-independent methods in quantum scattering theory.[1]

An alternative approach is to treat the dynamics of systems 2 and 3 by employing the recently developed ADMP formalism.[34,51,63–67] Here the electronic structure is represented by the single particle electronic density matrix and propagated simultaneously with the classical nuclei, with a simple adjustment of the relative nuclear and electronic time-scales. This is achieved within an extended Lagrangian formalism.[32,34,51,82,83] It has been shown that this dynamical strategy leads to a trajectory that oscillates about the Born–Oppenheimer surface with controllable deviations[51,64] and the results agree well with Born–Oppenheimer dynamics calculations.[63,67] ADMP has also been shown to be computationally superior to Born–Oppenheimer dynamics, and this is on account of the relaxation of SCF convergence requirement in ADMP.[63,66,67] (Please see Appendix for details in this regard.) The corresponding equations for the systems 2 and 3 are given by

$$\mathbf{M}\frac{d^2\mathbf{R_C}}{dt^2}=-\left\langle\chi\left|\left.\frac{\partial E(\{\mathbf{R_C},\mathbf{P_C}\},R_{\mathrm{QM}})}{\partial\mathbf{R_C}}\right|_{\mathbf{P_C}}\right|\chi\right\rangle, \tag{5}$$

and

$$\underline{\mu}^{1/2}\frac{d^2\mathbf{P_C}}{dt^2}\underline{\mu}^{1/2}=-\left\langle\chi\left|\left.\frac{\partial E(\{\mathbf{R_C},\mathbf{P_C}\},R_{\mathrm{QM}})}{\partial\mathbf{P_C}}\right|_{\mathbf{R_C}}\right|\chi\right\rangle - [\mathbf{\Lambda P_C}+\mathbf{P_C\Lambda}-\mathbf{\Lambda}], \tag{6}$$

where we have used χ instead of ψ_1 to describe the state of the quantum dynamical system 1. (For convenience, from this point on we use χ to represent the state of the quantum dynamical system, instead of ψ_1.) Here $\mathbf{M}$ denotes the classical nuclear masses in system 2 and $\underline{\mu}$ denotes a fictitious mass tensor or inertia tensor describing the effective electronic degrees of freedom. $\mathbf{\Lambda}$ is a Lagrangian multiplier matrix used to impose N-representability of the single particle

density matrix, $\mathbf{P_C}$. It is to be noted that Eq. (6) is classical in form, but not in content. Equations (5) and (6) are obtained by enforcing constraints of *N*-representability on the density matrix; the extended Lagrangian thus obtained, however, differs from that found in the standard time-dependent variational principle[69,84] and is hence a fictitious Lagrangian. Further discussion on the associated fictitious dynamics of the electrons can be found in Sec. II B with more details in Refs. 51 and 64.

Equation (2) retains its original form and is given explicitly as

$$\begin{aligned} \iota\hbar\frac{\partial}{\partial t}\chi(R_{\mathrm{QM}};t) &= \mathcal{H}_1\chi(R_{\mathrm{QM}};t) \\ &\equiv \left[-\frac{\hbar^2}{2M_{\mathrm{QM}}}\nabla^2_{R_{\mathrm{QM}}} + E(\{\mathbf{R_C},\mathbf{P_C}\},R_{\mathrm{QM}})\right] \\ &\quad\times\chi(R_{\mathrm{QM}};t). \end{aligned} \tag{7}$$

The energy functional, $E(\{\mathbf{R_C},\mathbf{P_C}\},R_{\mathrm{QM}})$, in Eqs. (5)–(7), depends on the quantum particle coordinates, R_{QM}, the surrounding classical nuclear coordinates, $\mathbf{R_C}$, and single particle electronic density matrix, $\mathbf{P_C}$, written in an orthonormal basis to be discussed further in the following. The energy, $E(\{\mathbf{R_C},\mathbf{P_C}\},R_{\mathrm{QM}})$, may be a density functional that involves exact exchange,[85] a pure functional[86] (with gradient corrections[87] or higher order corrections[88]) or may be based on other single particle formalisms such as Hartree–Fock or semiempirical treatments. It is written here using McWeeny purification[89] for the density matrix, $\tilde{\mathbf{P}}_\mathbf{C}=3\mathbf{P_C}^2-2\mathbf{P_C}^3$:

$$E = \mathrm{Tr}\left[\mathbf{h}\tilde{\mathbf{P}}_\mathbf{C} + \tfrac{1}{2}\mathbf{G}(\tilde{\mathbf{P}}_\mathbf{C})\tilde{\mathbf{P}}_\mathbf{C}\right] + E_{\mathrm{xc}} + V_{NN}. \tag{8}$$

Here, $\mathbf{h}$ is the one-electron matrix and $\mathbf{G}(\tilde{\mathbf{P}}_\mathbf{C})$ is the two-electron matrix for Hartree–Fock calculations, but for density functional theory (DFT) it represents the Coulomb potential. E_{xc} is the DFT exchange-correlation functional (for Hartree–Fock $E_{\mathrm{xc}}=0$) and V_{NN} represents the nuclear repulsion energy. Since the Gaussian basis set is employed in the ADMP formalism (this is by no means a requirement and density matrix propagation along identical lines can be formulated for other bases as well), the overlap matrix for the nonorthogonal Gaussian basis, $\mathbf{S}'$, may be factorized as $\mathbf{S}'=\mathbf{U}^\mathbf{T}\mathbf{U}$ to obtain the instantaneous orthonormal basis set.[90] There are a number of choices for $\mathbf{U};\mathbf{U}$ can be obtained from Cholesky decomposition[91] of $\mathbf{S}'$ or $\mathbf{U}=\mathbf{S}'^{1/2}$ for Löwdin symmetric orthogonalization. Further discussion on the *ab initio* molecular dynamics portion of the current algorithm is presented in Sec. II B.

A. Quantum wave packet propagation

The quantum-dynamical propagation, based on Eq. (7), is approximated using a kinetic reference symmetric split operator approach:[5,92]

$$\begin{aligned} \exp\left\{-\frac{\iota Ht}{\hbar}\right\} &= \exp\left\{-\frac{\iota Vt}{2\hbar}\right\}\exp\left\{-\frac{\iota Kt}{\hbar}\right\}\exp\left\{-\frac{\iota Vt}{2\hbar}\right\} \\ &\quad + \mathcal{O}(t^3), \end{aligned} \tag{9}$$

where *K* is the kinetic energy operator of Eq. (7) and the *V* is the (local) potential energy operator. This approach has the attractive feature that it provides dynamics strictly obeying time-reversal symmetry[5,92] if the approximations used for the separate components of Eq. (9) are unitary.

For local potentials, the potential energy operator is diagonal in the coordinate representation. There are a number of ways to approximate the free-propagator, $\exp\{-\iota Kt/\hbar\}$. One approach is to recognize that this operator is diagonal in the momentum representation. Hence fast Fourier transforms have been commonly used[5,8,19–22] to obtain the result of the free-propagator operating on a wave packet in the coordinate representation. A few alternative approaches include: (a) the use of direct[25] or iterative, Lanczos[7] based diagonalization of the full Hamiltonian and the subsequent representation of the evolution operator $\exp\{-\iota Ht/\hbar\}$ using the eigenstates, (b) the use of Chebychev polynomial approximations[6,11,23–25,93] which are based on the Jacobi–Anger formula,[94] (c) use of eigenstates of various portions of the Hamiltonian,[95] and (d) the use of Feynman path integrals.[12–15,96–99] (The list here is not exhaustive and a detailed discussion on the topic may be found in Refs. 1 and 35.) In all cases, the Hamiltonian needs to be approximated in some representation. In the coordinate representation this is generally achieved with the discrete-variable representations[26–28] or distributed approximating functionals (DAF).[53,54,57,100–102]

In the current study we employ an analytic banded DAF[53,55] representation for the coordinate space version of the free-propagator:

$$\begin{aligned} &\left\langle R_{\mathrm{QM}}\left|\exp\left\{-\frac{\iota K\Delta t_{\mathrm{QM}}}{\hbar}\right\}\right|R'_{\mathrm{QM}}\right\rangle_{\mathrm{DAF}} \\ &\quad= \frac{1}{\sigma(0)}\exp\left\{-\frac{(R_{\mathrm{QM}}-R'_{\mathrm{QM}})^2}{2\sigma(\Delta t_{\mathrm{QM}})^2}\right\} \\ &\qquad\times\sum_{n=0}^{M/2}\left(\frac{\sigma(0)}{\sigma(\Delta t_{\mathrm{QM}})}\right)^{2n+1}\left(\frac{-1}{4}\right)^n\frac{1}{n!}(2\pi)^{-1/2} \\ &\qquad\times H_{2n}\left(\frac{R_{\mathrm{QM}}-R'_{\mathrm{QM}}}{\sqrt{2}\sigma(\Delta t_{\mathrm{QM}})}\right), \end{aligned} \tag{10}$$

where

$$\{\sigma(\Delta t_{\mathrm{QM}})\}^2 = \sigma(0)^2 + \frac{\iota\Delta t_{\mathrm{QM}}\hbar}{M_{\mathrm{QM}}} \tag{11}$$

and $H_{2n}(x)$ are the Hermite polynomials of even order. Equation (10) is obtained from the well-known analytical expression for free evolution of a Gaussian function,[96]

$$\begin{aligned} &\exp\left\{-\frac{\iota K\Delta t_{\mathrm{QM}}}{\hbar}\right\}\exp\left[-\frac{x^2}{2\sigma(0)^2}\right] \\ &\quad= \frac{\sigma(0)}{\sigma(\Delta t_{\mathrm{QM}})}\exp\left[-\frac{x^2}{2\sigma(\Delta t_{\mathrm{QM}})^2}\right] \end{aligned} \tag{12}$$

along with the fact that the Hermite functions are generated from Gaussians according to

$$H_n(x)\exp\left[-\frac{x^2}{2\sigma^2}\right] = (-1)^n \frac{d^n}{dx^n}\exp\left[-\frac{x^2}{2\sigma^2}\right]. \tag{13}$$

Since the derivative operators d^n/dx^n commute with the free-propagator, the Hermite functions can be used as a basis to expand the exact quantum free propagator with coefficients as described in Eq. (10).[53] This yields an efficient propagation scheme to perform quantum dynamics and Feynman path integration[96,97] through the action of a banded, sparse, Toeplitz matrix on a vector.

For the rest of this section we will briefly describe DAF quantum propagator theory as it pertains to the current wave packet *ab initio* dynamics approach. Further details on DAF theory can be found in Refs. 29, 53, and 55–57

Equation (10) is presented in its continuous form and is valid for all values of R_{QM} and R'_{QM}. Here the free evolution of a wave packet $\chi(R_{\mathrm{QM}};t)$ is obtained by discretization:

$$\chi(R_{\mathrm{QM}};t+\Delta t) = \int dR'_{\mathrm{QM}} \left\langle R_{\mathrm{QM}} \left| \exp\left\{-\frac{\imath K \Delta t_{\mathrm{QM}}}{\hbar}\right\} \right| R'_{\mathrm{QM}} \right\rangle_{\mathrm{DAF}} \chi(R'_{\mathrm{QM}};t),$$

$$\chi(R^i_{\mathrm{QM}};t+\Delta t) = \frac{\Delta x}{\sigma(0)} \sum_j \exp\left\{-\frac{(R^i_{\mathrm{QM}}-R^j_{\mathrm{QM}})^2}{2\sigma(\Delta t_{\mathrm{QM}})^2}\right\} \sum_{n=0}^{M/2} \left(\frac{\sigma(0)}{\sigma(\Delta t_{\mathrm{QM}})}\right)^{2n+1} \times \left(\frac{-1}{4}\right)^n \frac{1}{n!} (2\pi)^{-1/2} H_{2n}\left(\frac{R^i_{\mathrm{QM}}-R^j_{\mathrm{QM}}}{\sqrt{2}\sigma(\Delta t_{\mathrm{QM}})}\right) \chi(R^j_{\mathrm{QM}};t), \tag{14}$$

where Δx is the grid discretization (assumed uniform in this case) in one dimension. Generalization to higher dimensions is straightforward and is carried out by writing the propagator in direct product form with components as in Eq. (10). The variables M and $\sigma(0)$ determine the accuracy and width (or computational efficiency), respectively, of the DAF. It has been shown[53,57] that these parameters are not independent and that for a given value of M there exists a $\sigma(0)$ that provides optimal accuracy for the propagation. We have studied the accuracy of the quantum propagation in Sec. III using a variety of values for M and $\sigma(0)$, to demonstrate the convergence of our results with DAF parameters. The values used in our study are listed in Sec. III and are based on the requirement of optimal accuracy as discussed in Ref. 53. In the computational section of this paper, we have also discussed comparison of this propagation scheme with a propagation obtained from exact diagonalization of the Hamiltonian, $\mathcal{H}_1$ in Eq. (7). This provides a useful benchmark of our results.

To calculate the Hermite polynomials in Eq. (10), the standard recursion procedure can be used, however, for large values of M (which leads to greater accuracy of the propagation), these polynomials numerically diverge. As a result we have modified the recursion relation to allow the direct evaluation of the functions

$$\tilde{H}_{2n}\left(\frac{x}{\sqrt{2}\sigma}\right) = \exp\left\{-\frac{x^2}{2\sigma^2}\right\} \frac{1}{n!} H_{2n}\left(\frac{x}{\sqrt{2}\sigma}\right), \tag{15}$$

using

$$\tilde{H}_{2n}(y) = \frac{2}{n}[(2y^2-4n+3)\tilde{H}_{2n-2}(y) - 4(2n-3)\tilde{H}_{2n-4}(y)]. \tag{16}$$

Equation (16) only includes the even polynomials as needed in Eq. (10). This modified recursion allows numerically stable evaluation of the components required in Eq. (10) even for very large values of M.

It is worth noting a few characteristics of Eq. (10). For any fixed level of approximation, determined by the choice of parameters M and $\sigma(0)$, the kernel in Eq. (10) only depends on the quantity $(R_{\mathrm{QM}}-R'_{\mathrm{QM}})$ (that is the distance between points in the coordinate representation) and goes to zero as this quantity becomes numerically large on account of the Gaussian dependence. This yields a banded matrix approximation to Eq. (10), for any finite M and $\sigma(0)$. Furthermore, on account of its dependence on $(R_{\mathrm{QM}}-R'_{\mathrm{QM}})$, a matrix representation of Eq. (10) has the property that all diagonal elements of this matrix are equal; similarly all nth super (and sub) diagonal elements are the same. Such a matrix is called a Toeplitz matrix. [One may note that the Toeplitz matrix is very similar to the Vandemonde matrix that makes its appearance in Fourier theory. [91] This is no surprise since the exact quantum propagator in the coordinate representation[96] is obtained by representing the free-propagator in the momentum representation. Furthermore, the matrix representation of Eq. (10) becomes a Vandemonde matrix when a symmetry adaptation scheme[103] is introduced and this will be discussed as part of a future study[104] of the methodology described in this paper.] In addition, the dependence on $(R_{\mathrm{QM}}-R'_{\mathrm{QM}})$ implies a translational symmetry property in Eq. (10), seemingly reminiscent of wavelet theories.[105–108] On account of such attractive mathematical properties, Eq. (10) provides great simplicity in computation of the quantum propagation within our scheme and is expected to be useful for large systems. For example, it is only necessary to store the first row of such a matrix, in each dimension, to obtain the result of a propagation. Furthermore, the computational scaling of the quantum propagation described in Eq. (14) is $\{(2W+1)(N-W)-W^2\}$, where N is the number of grid points used in the discretization scheme and $(2W+1)$ is the width of the propagator in the coordinate representation. Since W does not depend on N [W in fact depends on M and $\sigma(0)$, that is the required accuracy of propagation], this scaling goes as $\mathcal{O}(N)$ for large grids.

Another important property of the expression in Eq. (10) is that it is not formally unitary. This, however, does not present any problems in the numerical propagation as will be discussed in the results section. The reason for the lack of formal unitarity can be understood by considering the $\Delta t_{\mathrm{QM}} \to 0$ limit of Eq. (10). It is true that for the free propagator

$$\lim_{\Delta t_{\mathrm{QM}}\to 0} \left\langle x \left| \exp\left[-\frac{\imath K \Delta t_{\mathrm{QM}}}{\hbar}\right] \right| x' \right\rangle \equiv \delta(x-x'), \tag{17}$$

where the right-hand side is a projection operator in the following sense:

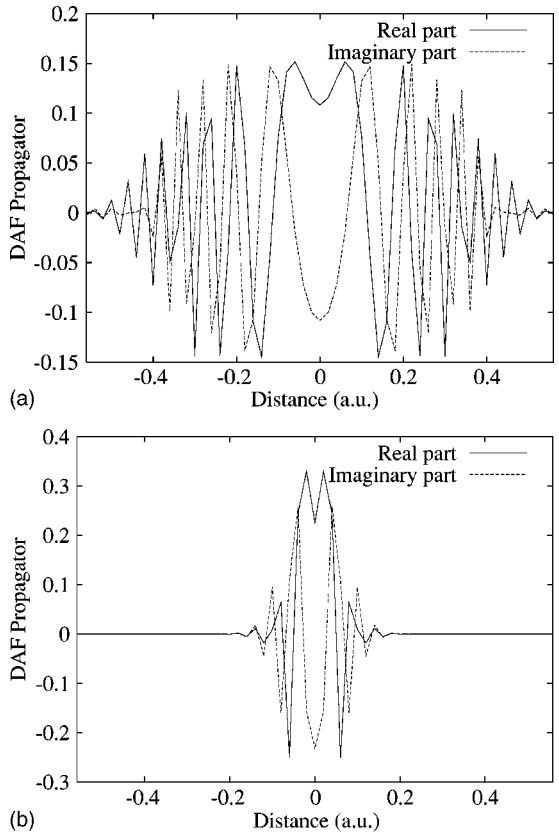

FIG. 1. DAF propagator in Eq. (10) for (a) $\Delta t=5$ a.u. and (b) $\Delta t=1$ a.u. $M=20$ and $\sigma(0)/\Delta x=1.5744$ for both cases.

$$\int \delta(x-x')\,\delta(x'-x'')dx' \equiv \delta(x-x''). \tag{18}$$

For the approximation in Eq. (10), this becomes an exact result only for large values of M, since the DAF-approximation, $\delta_{\mathrm{DAF}}(x-x')$:

$$\lim_{\Delta t_{\mathrm{QM}}\to 0}\left\langle x\left|\exp\left[-\frac{\imath K\Delta t_{\mathrm{QM}}}{\hbar}\right]\right|x'\right\rangle_{\mathrm{DAF}} \equiv \delta_{\mathrm{DAF}}(x-x') \approx \delta(x-x'), \tag{19}$$

is generally not a projection operator[109] in the sense of Eq. (18). The computational implications of this result are discussed in Sec. III A and found to be negligible.

Finally, we illustrate the form of the DAF propagator in Fig. 1 for two different time steps. As can be seen, the propagator gets broader in the coordinate representation, just by increasing the time step, even when the order of the approximation [determined by the choice of M and $\sigma(0)$] is maintained. This is particularly interesting since the current approach allows for an adaptive control of quantum time steps, based on energy conservation, and in such cases when the time step is increased more points in the vicinity of $\chi(x)$ contribute to its propagation. This aspect is further highlighted by considering the momentum space form of the DAF propagator:

$$\frac{1}{\sqrt{2}\sigma(\Delta t_{\mathrm{QM}})}\exp\left\{-\frac{k^2\sigma(\Delta t_{\mathrm{QM}})^2}{4}\right\}\sum_{n=0}^{M/2}\frac{2^n}{n!}[\sigma(0)k]^{2n}, \tag{20}$$

which is basically a polynomial multiplied by a coherent state,

$$\exp\left\{-\frac{k^2\sigma(\Delta t_{\mathrm{QM}})^2}{4}\right\} \equiv \exp\left\{-\frac{k^2}{4}(\sigma(0)^2+\imath\Delta t_{\mathrm{QM}}\hbar/M_{\mathrm{QM}})\right\}.$$

As can be seen, the plane wave frequency in the coherent state is time-step dependent, which implies that for larger time steps [but fixed M and $\sigma(0)$] the plane-wave portion of the Fourier transform of Eq. (10) becomes oscillatory for a given k. This is particularly interesting since coherent states have been used to propagate quantum systems,[110–113] but in our case the propagator in the momentum representation is a coherent state multiplied by a polynomial.

B. *Ab initio* dynamics using ADMP and Born–Oppenheimer dynamics

The ADMP approach has been discussed in great detail in Refs. 34, 51, and 63–67. In this section we present a brief outline as it pertains to the current quantum wave packet *ab initio* dynamics approach. The ADMP equations, (5) and (6), are propagated using the velocity Verlet algorithm:

$$\mathbf{P}_C^{i+1} = \mathbf{P}_C^i + \dot{\mathbf{P}}_C^i\Delta t - \frac{\Delta t^2}{2}\underline{\mu}^{-1/2} \times[\mathcal{F}^i_{\mathbf{P_C}} + \mathbf{\Lambda}_i\mathbf{P}_C^i + \mathbf{P}_C^i\mathbf{\Lambda}_i - \mathbf{\Lambda}_i]\underline{\mu}^{-1/2}, \tag{21}$$

$$\dot{\mathbf{P}}_C^{i+1} = \dot{\mathbf{P}}_C^i - \frac{\Delta t}{2}\underline{\mu}^{-1/2}[\{\mathcal{F}^i_{\mathbf{P_C}} + \mathbf{\Lambda}_i\mathbf{P}_C^i + \mathbf{P}_C^i\mathbf{\Lambda}_i - \mathbf{\Lambda}_i\} + \{\mathcal{F}^{i+1}_{\mathbf{P_C}} + \mathbf{\Lambda}_{i+1}\mathbf{P}_C^{i+1} + \mathbf{P}_C^{i+1}\mathbf{\Lambda}_{i+1} - \mathbf{\Lambda}_{i+1}\}]\underline{\mu}^{-1/2}, \tag{22}$$

with

$$\mathcal{F}^i_{\mathbf{P_C}} = \left\langle\chi\left|\left.\frac{\partial E(\{\mathbf{R_C},\mathbf{P_C}\},R_{\mathrm{QM}})}{\partial\mathbf{P}_{\mathrm{C}}}\right|_{\mathbf{R}_{\mathrm{C}}}\right|\chi\right\rangle. \tag{23}$$

Similarly, the nuclei are propagated according to

$$\mathbf{R}_C^{i+1} = \mathbf{R}_C^i + \dot{\mathbf{R}}_C^i\Delta t - \frac{\Delta t^2}{2}\mathbf{M}^{-1/2}\mathcal{F}^i_{\mathbf{R_C}}\mathbf{M}^{-1/2}, \tag{24}$$

$$\dot{\mathbf{R}}_C^{i+1} = \dot{\mathbf{R}}_C^i - \frac{\Delta t}{2}\mathbf{M}^{-1/2}[\mathcal{F}^i_{\mathbf{R_C}} + \mathcal{F}^{i+1}_{\mathbf{R_C}}]\mathbf{M}^{-1/2}, \tag{25}$$

where $\dot{\mathbf{R}}_C^i$ are the nuclear velocity at time step i and

$$\mathcal{F}^i_{\mathbf{R_C}} = \left\langle\chi\left|\left.\frac{\partial E(\{\mathbf{R_C},\mathbf{P_C}\},R_{\mathrm{QM}})}{\partial\mathbf{R_C}}\right|_{\mathbf{P}_{\mathrm{C}}}\right|\chi\right\rangle. \tag{26}$$

Equations (23) and (26) represent the essential difference in the current methodology as compared to standard ADMP since the forces here are averaged over the quantum wave packet as required from the discussion in Sec. II.

If Born–Oppenheimer dynamics is to be used instead of ADMP, Eq. (6) is replaced by SCF convergence of $\mathbf{P_C}$. The nuclear propagation equation remains the same in both formalisms. However, the nuclear forces are different since the ADMP nuclear forces are more general than the standard Born–Oppenheimer dynamics nuclear forces[34,64] and the difference between these is proportional to the commutator of the Fock and density matrices[64] that is generally small in Born–Oppenheimer dynamics (when the SCF convergence threshold is tight) but may not be small in ADMP:

$$\begin{aligned}\left.\frac{\partial E(\{\mathbf{R_C},\mathbf{P_C}\},R_{\mathrm{QM}})}{\partial \mathbf{R_C}}\right|_{\mathbf{P_C}} &= \left\{ \mathrm{Tr}\left[\frac{d\mathbf{h}'}{d\mathbf{R_C}}\tilde{\mathbf{P}}'_{\mathbf{C}} + \frac{1}{2}\frac{\partial \mathbf{G}'(\mathbf{P}'_{\mathbf{C}})}{\partial \mathbf{R_C}}\bigg|_{\mathbf{P}'_{\mathbf{C}}}\tilde{\mathbf{P}}'_{\mathbf{C}}\right] \right. \\ &\quad \left. - \mathrm{Tr}\left[\mathbf{F}'\tilde{\mathbf{P}}'_{\mathbf{C}}\frac{d\mathbf{S}'}{d\mathbf{R_C}}\tilde{\mathbf{P}}'_{\mathbf{C}}\right] + \left.\frac{\partial E_{\mathrm{xc}}}{\partial \mathbf{R_C}}\right|_{\mathbf{P_C}} + \frac{\partial V_{NN}}{\partial \mathbf{R_C}}\right\} \\ &\quad + \mathrm{Tr}\left[[\tilde{\mathbf{P}}_{\mathbf{C}},\mathbf{F}]\left(\tilde{\mathbf{Q}}_{\mathbf{C}}\frac{d\mathbf{U}}{d\mathbf{R_C}}\mathbf{U}^{-1} - \tilde{\mathbf{P}}_{\mathbf{C}}\mathbf{U}^{-\mathbf{T}}\frac{d\mathbf{U}^{\mathbf{T}}}{d\mathbf{R_C}}\right)\right], \end{aligned} \tag{27}$$

where $\tilde{\mathbf{Q}}_{\mathbf{C}} \equiv \mathbf{I} - \tilde{\mathbf{P}}_{\mathbf{C}}$ and as noted in Eq. (8), $\tilde{\mathbf{P}}_{\mathbf{C}}$ is the McWeeny purified density matrix. Notice that as the commutator of the Fock and density matrices goes to zero, the last term in Eq. (27) becomes small leading to well-known gradient expressions.[34,64,114] [The primed variables in Eq. (27) are in the nonorthogonal Gaussian basis.[34,64]] In the absence of this condition, Eq. (27) presents a more general form of the nuclear gradient and we use this for both cases, especially for the case of weak convergence threshold on the Born–Oppenheimer surface. The density matrix gradient in Eq. (6) is given by

$$\begin{aligned}\left.\frac{\partial E(\{\mathbf{R_C},\mathbf{P_C}\},R_{\mathrm{QM}})}{\partial \mathbf{P_C}}\right|_{\mathbf{R_C}} &= 3\mathbf{F}\mathbf{P_C} + 3\mathbf{P_C}\mathbf{F} - 2\mathbf{F}\mathbf{P_C}^2 - 2\mathbf{P_C}\mathbf{F}\mathbf{P_C} - 2\mathbf{P_C}^2\mathbf{F} \\ &\equiv [[\mathbf{F},\mathbf{P_C}],\mathbf{P_C}]. \end{aligned} \tag{28}$$

Equation (6) is similar to that used in the Car-Parrinello (CP) scheme however, it differs importantly in using the single particle density matrix in an orthonormal basis set formed from Gaussian basis functions. In this sense Eq. (6) represents fictitious dynamics (like CP), where the density matrix is propagated instead of being converged [as would be required if the time-independent Schrödinger equation were used instead of Eq. (6)]. The accuracy and efficiency of ADMP is controlled by the choice of $\underline{\mu}$. Hence one must be aware of the limits on this quantity. Two criteria[51,64] have been derived to place bounds on the choice of the fictitious mass. First, the choice of the fictitious mass determines the magnitude of the commutator $[\mathbf{P_C},\mathbf{F}]$ (where $\mathbf{F}$ is the Fock matrix that represents the single particle picture; DFT, Hartree–Fock, or semiempirical) thus determining the extent of deviation from the Born-Oppenheimer surface:[64]

$$\|[\mathbf{F},\mathbf{P_C}]\|_F \geqslant \frac{1}{\|[\mathbf{P_C},\dot{\mathbf{P}}_{\mathbf{C}}]\|_F}|\mathrm{Tr}[\dot{\mathbf{P}}_{\mathbf{C}}\underline{\mu}^{1/2}\ddot{\mathbf{P}}_{\mathrm{C}}\underline{\mu}^{1/2}]|, \tag{29}$$

where $\|[\cdots]\|_F$ is the Frobenius norm[91,115] of the commutator and is defined as $\|A\|_F = \sqrt{\Sigma_{i,j}A_{i,j}^2}$. $\dot{\mathbf{P}}_C$ and $\ddot{\mathbf{P}}_C$ are *velocity* and *acceleration* of the density matrix and can be determined on the fly as outlined in the propagation scheme described in the following. Second, the rate of change of the fictitious kinetic energy,

$$\begin{aligned}\frac{d\mathcal{H}_{\mathrm{fict}}}{dt} &= \mathrm{Tr}[\dot{\mathbf{P}}_{\mathbf{C}}\underline{\mu}^{1/2}\ddot{\mathbf{P}}_{\mathbf{C}}\underline{\mu}^{1/2}] \\ &= -\mathrm{Tr}\left[\dot{\mathbf{P}}_{\mathbf{C}}\left(\left.\frac{\partial E(\mathbf{R_C},\mathbf{P_C})}{\partial \mathbf{P_C}}\right|_{\mathbf{R_C}} + \mathbf{\Lambda}\mathbf{P_C} + \mathbf{P_C}\mathbf{\Lambda} - \mathbf{\Lambda}\right)\right], \end{aligned} \tag{30}$$

is *required to be bounded and oscillatory* and this again is determined by the choice of fictitious mass tensor. Note that the numerator in Eq. (29) is the same as the expression in Eq. (30) and hence this implies that the rate of change of the fictitious kinetic energy in ADMP is also proportional to the commutator $[\mathbf{P_C},\mathbf{F}]$ and hence determines deviations from the Born–Oppenheimer surface. One must monitor the quantities in Eqs. (29) and (30) to ascertain that the ADMP portion of the dynamics is physically consistent. In all ADMP applications studied to date[34,51,63,66,116–118] these conditions are satisfied thus yielding a computationally efficient and accurate approach to model dynamics on the Born–Oppenheimer surface. It has been shown that ADMP trajectories thus obtained are in good agreement with dynamics on the Born–Oppenheimer surface.[63,67]

C. Computational implementation

The algorithm to perform the simultaneous dynamics of the $\{\mathbf{R_C},\mathbf{P_C},\chi\}$ system is described as follows: First a grid is created around the particle to be treated quantum dynamically. This grid represents the discretization of the wave packet, χ, in the coordinate representation. If the ADMP dynamics option is desired, the potential energy $E(\{\mathbf{R_C},\mathbf{P_C}\},R_{\mathrm{QM}})$, the nuclear forces,

$$\left.\frac{\partial E(\{\mathbf{R_C},\mathbf{P_C}\},R_{\mathrm{QM}})}{\partial \mathbf{R_C}}\right|_{\mathbf{P_C}}$$

and density matrix forces,

$$\left.\frac{\partial E(\{\mathbf{R_C},\mathbf{P_C}\},R_{\mathrm{QM}})}{\partial \mathbf{P_C}}\right|_{\mathbf{R_C}},$$

are calculated on the grid points. On the contrary if Born–Oppenheimer dynamics is the chosen approach, then the potential energy and only classical nuclear forces are obtained based on SCF convergence. This is an important difference and clearly indicates the lower computational effort required in ADMP. (The Appendix explains this in detail and as will be seen in Sec. III B the associated loss in accuracy is basically negligible.)

The potential energy on the grid along with the free propagator in Eq. (10) are then used for causal propagation

of the quantum wave packet. The energy gradients on the grid points are used along with the wave packet to construct the force on the ADMP system as required by Eqs. (23) and (26), which propagates the ADMP variables: $\{\mathbf{R_C}, \mathbf{P_C}\}$ and the associated velocities $\{\dot{\mathbf{R}}_\mathbf{C}, \dot{\mathbf{P}}_\mathbf{C}\}$, as allowed by Eqs. (21), (22), (24), and (25). (Only the nuclear degrees of freedom are propagated for the Born–Oppenheimer case.) This process is then repeated for the next propagation step.

The above-presented algorithm is, of course, limited by the size of the quantum grid and to facilitate maximum compactness, we use an adaptive grid methodology wherein the required grid positions are recalculated every few time steps based on the center and instantaneous distribution of the wave packet. The wave packet amplitudes at the new grid positions are calculated with an accurate grid interpolation scheme:[54,100,103,119,120]

$$\chi(R_{\mathrm{QM}};t) = \int dR'_{\mathrm{QM}} \left\{ \frac{1}{\sigma\sqrt{2\pi}} \exp\left(-\frac{(R_{\mathrm{QM}} - R'_{\mathrm{QM}})^2}{2\sigma^2} \right) \times \sum_{n=0}^{M/2} \left(-\frac{1}{4} \right)^n \frac{1}{n!} H_{2n}\left(\frac{R_{\mathrm{QM}} - R'_{\mathrm{QM}}}{\sqrt{2}\sigma} \right) \right\} \chi(R'_{\mathrm{QM}};t), \tag{31}$$

to transform the wave packet from the primed (old) set of grid points to the unprimed (new) set. This way the quantum grid adapts to the region where the quantum wave packet has significant contributions. Equation (31) also allows us the adjustment of wave packet grid sampling by having more points in regions where the wave packet is rapidly varying. This sampling is maintained based on predetermined factors such as de Broglie wavelength of the quantum particle or local, instantaneous gradient and curvature of the potential surface.[121,122] The adaptive nature of the quantum grid makes the approach robust. It is also important to note that the computationally expensive portion of the algorithm described here is the evaluation of the energy and forces on the grid points to be used for ADMP dynamics. This necessitates a reduction of the number of grid points where such calculations are performed and we are currently developing a scheme that involves potential adapted interpolation to minimize the number of grid points where such calculations are performed. Exhaustive discussion of these novel extensions to the methodology and detailed examination of grid sizes and other computational aspects will be the subject of a future publication.[122] In the current contribution we focus on the accuracy, efficiency, and complete evaluation of the parameters involved in the proposed methodology.

Another important factor in the quantum propagation scheme is related to the nature of the discretized DAF propagator in Eq. (14). Equation (14) may be interpreted as a matrix-vector multiplication where the $(R^i_{\mathrm{QM}}, R^j_{\mathrm{QM}})$th element of the propagator matrix acts on the initial vector to create the new vector. In this case, we note that for points near the edges of the grid defined by $[i \leqslant W]$ and $[N-i \leqslant W]$, where $R^i_{\mathrm{QM}} \equiv i\Delta x$, N is the number of grid discretization points and $(2W+1)$ is the width of the DAF propagator in the coordinate representation, there is an error in the discretization scheme in Eq. (14) due to the fact that

$$\left\langle R^i_{\mathrm{QM}} \left| \exp\left\{ -\frac{\iota K \Delta t_{\mathrm{QM}}}{\hbar} \right\} \right| R^j_{\mathrm{QM}} \right\rangle_{\mathrm{DAF}}$$

is nonzero for $[i \leqslant W]$ and $j < 0$. That is, the DAF propagator extends beyond the region of definition of the grid on either side! However, the size of this extended region is proportional to $W\Delta x$. Now, one of the properties of the DAF propagator is that its bandwidth, W, is independent of the grid size Δx (although it does depend on the time step Δt, as seen in Fig. 1) as long as the values of $\sigma(0)$ and M are kept constant.[103] Hence, as Δx is made smaller, the total number of grid points, N, increases and the ratio $W/N(\propto \Delta x)$ gets smaller. Hence, as the grid spacing is reduced, the size of the above-described extended region gets smaller and in the continuous limit, i.e., as Δx becomes infinitesimally small, this region, $W/N \propto \Delta x$, becomes infinitesimally small. For finite size grid spacings the numerical effects of this problem at grid boundaries is reduced using a symmetry-adapted version of the propagator scheme and will be the subject of future studies.[104]

III. DISCUSSION OF NUMERICAL TESTS

To conduct an exhaustive study of the parameters in the proposed methodology and to test the accuracy of the approach we have performed many sets of calculations; an illustrative sample is discussed here. In the first set of calculations we compare the quantum dynamics obtained for the shared proton in the $Cl_2^{2-}H^+$ system using two different *time-independent* potential energy surfaces: in one case full SCF (with a wave function convergence threshold of 10^{-8} which translates to an energy convergence threshold of roughly 10^{-10} hartree) was used to construct the potential surface [as would be the case in the Born–Oppenheimer (BO) dynamics implementation of the proposed methodology] and in the other case a single SCF cycle was used to estimate the energy surface as would be the case for ADMP. In both cases the chloride atomic positions are fixed. In all cases the electronic structure was determined from density functional theory, using pure and hybrid functionals. We carefully checked sensitivity of the quantum dynamics with respect to the parameters including the quantum time step and values of DAF-free propagator parameters, M and the associated $\sigma(0)$. Use of a single time-independent potential energy surface during the course of propagation allows us to compare and calibrate the DAF-based propagation approach with results obtained from exact propagation via diagonalization of the Hamiltonian. The instantaneous quantum wave packet in the exact case is simply a linear combination of the stationary eigenstates of the Hamiltonian multiplied by energy-dependent phase factors:

$$|\chi(t)\rangle_{\mathrm{exact}} = \sum_i c_i^{\mathrm{exact}}(t)|\phi_i\rangle = \sum_i c_i(0)\exp[-\iota E_i t/\hbar]|\phi_i\rangle \tag{32}$$

where the eigenstates $\{\phi_i\}$ are obtained from exact diagonalization of the Hamiltonian in Eq. (7):

$$\left[-\frac{\hbar^2}{2M_{\mathrm{QM}}}\nabla^2_{R_{\mathrm{QM}}}+E(\{\mathbf{R_C},\mathbf{P_C}\},R_{\mathrm{QM}})\right]|\phi_i\rangle=E_i|\phi_i\rangle. \quad (33)$$

These eigenvalues and eigenvectors were determined using two different methods to confirm our results: (a) first the Numerov approach[123] to boundary value problems[124] was used to determine the eigenvalues and eigenvectors, (b) next the kinetic energy operator was obtained in the coordinate representation using "distributed approximating functional"[11,25,29,53,54,57,100] and the Hamiltonian was subsequently diagonalized. In both cases the eigenvalues and eigenvectors were found to be in very good agreement. Hence we proceeded to use these eigenstates to benchmark our results as described in the following.

The DAF-propagated wave packet could, in a similar fashion, be resolved as

$$|\chi(t)\rangle_{\mathrm{DAF}}=\sum_i c_i^{\mathrm{DAF}}(t)|\phi_i\rangle \quad (34)$$

to provide a platform for comparing our results. A range of applicable DAF parameters have been tested for accuracy. A smaller number M does allow a reduction in the CPU time for quantum propagation, although this is not the computationally critical portion of the full method. We have performed this comparison to evaluate the accuracy of our wave packet dynamics scheme for both the ADMP and BO cases. The results from this comparison are presented in Sec. III A. After checking accuracy of quantum propagation for fixed potential energy surfaces the chloride atoms and the electrons are allowed to evolve as per ADMP or Born–Oppenheimer dynamics simultaneously with the quantum wave packet. This is used to test the full methodology and the results obtained are presented in Sec. III B.

Another set of tests is dedicated to the study of a proton tunneling problem for a more computationally intensive case to demonstrate the potential applications of this approach. In Sec. III C the dynamics of a "quantum-proton" between a phenol and tri-methyl amine system is studied and comparisons between different density functionals are presented.

A. Accuracy of quantum propagation

We have conducted simulations for the $Cl_2^{2-}H^+$ system to test the accuracy of our quantum propagation. The wave packet approach outlined in the previous section has been used to study the quantum dynamics representing the shared proton. Hybrid density functional theory (B3LYP) with a 6-31*G* Gaussian basis was used for all electronic calculations discussed in this section.

We consider the quantum dynamics of the shared proton in the $Cl_2^{2-}H^+$ system with the chloride ions fixed at about 4.2 Å separation and the initial wave packet, chosen to be a Gaussian. While the 4.2 Å starting geometry is one among many geometries that we considered, it is useful to discuss this geometry to exemplify the implications of our numerical tests. First, at this geometry, the zero-point energy of the proton is rather high and comparable to the height of the barrier that separates the protonated states on each chloride ion. (The zero-point energy is approximately 2 millihartrees and the height of the barrier is close to 4 millihartrees.) This gives rise to the possibility of tunneling *and* zero point effects playing an important role in the dynamics if the initial wave packet is chosen to have a finite overlap with the proton ground state. In addition there are multiple states accessible for tunneling below the barrier. Such physical situations have been termed "nonadiabatic" in the proton transfer literature.[68] The other interesting aspect of this geometry is the proximity of states immediately above the barrier which provides for a high probability of over-barrier reflection of the wave packet if the initial packet has finite overlap with these over-barrier states. It must be noted that most methodologies that study quantum dynamics in large systems[125,126] do not adequately reproduce all three effects. While many methods accurately reproduce the zero-point effects, few are able to reproduce both tunneling and over-barrier reflection accurately. It is also worthwhile to note that the standard semiclassical approximation[73] breaks down in the vicinity of barrier height, which provides the rationale for a fully quantum dynamical approach.

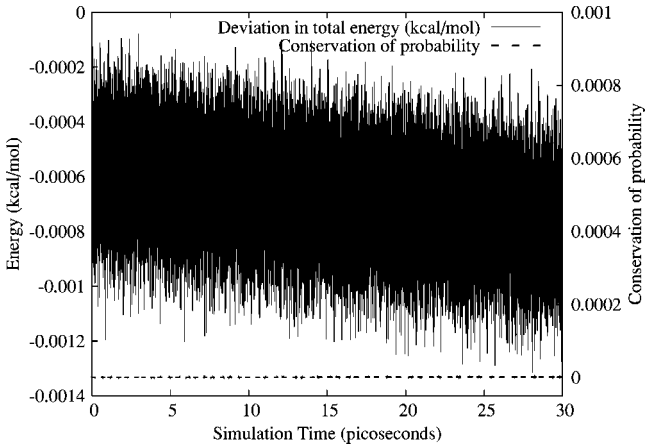

FIG. 2. Conservation of total energy and probability are presented for a 30 ps quantum dynamics simulation. The deviations in total energy (oscillatory curve) are in the microhartree range. The conservation of probability flux (flat dashed line), outlined in Eq. (36), is also more than adequate. Calculations are performed using $M=60$.

To test our scheme with reference to all three quantum dynamical aspects described earlier, we have constructed the initial wave packet as a Gaussian having finite overlap with states all the way from the ground state to states a few millihartrees above the barrier:

$$|\chi(0)\rangle\equiv\exp[-x^2/(2\alpha^2)]=\sum_i c_i(0)|\phi_i\rangle. \quad (35)$$

The quantum propagation is performed using the DAF expression in Eq. (10) and, to calibrate the approach, these results are compared with the exact propagation in Eq. (32).

We first assess the numerical effects of the formal nonunitarity of the DAF propagation scheme. A serious loss in unitarity could result in many unphysical results: for example, (a) loss in energy conservation during the dynamics process, (b) loss of probability, (c) the coefficients may not strictly obey, or may deviate substantially from, the result of Eq. (32), and (d) loss of time-reversal symmetry which is one of the cornerstones of the split-operator approximation.[96,127,128] In Fig. 2 we present the evolution of

TABLE I. Propagation error, as calculated from Eq. (38), for different values of DAF parameters. The simulations with $\Delta t=0.1$ fs were 10 ps long while the $\Delta t=0.5$ fs simulations were 40 ps long.

PES	Δt(fs)	$M=10\ \frac{\sigma(0)}{\Delta x}=1.1805$	$M=20\ \frac{\sigma(0)}{\Delta x}=1.5744$	$M=30\ \frac{\sigma(0)}{\Delta x}=1.8800$	$M=40\ \frac{\sigma(0)}{\Delta x}=2.1387$	$M=60\ \frac{\sigma(0)}{\Delta x}=2.5742$
BO	0.1	0.002 312 9	0.000 495 5	0.000 493 9	0.000 494 3	0.000 493 9
ADMP	0.1	0.001 976 3	0.000 404 4	0.000 403 0	0.000 403 4	0.000 403 0
BO	0.5	0.014 671 2	0.014 700 9	0.014 700 9	0.014 701 2	0.014 700 8
ADMP	0.5	0.012 762 5	0.012 768 5	0.012 768 3	0.012 769 2	0.012 768 2

the total energy and loss of wave packet probability as a function of time. We note that the total energy is conserved to beyond microhartree accuracy over a 30 ps simulation time. (Note that the vertical axis in Fig. 2 is such that the energy has units of kcal/mol.) Similarly the loss of wave packet probability in the DAF propagation,

$$\frac{1}{N}\sqrt{\sum_{i}^{N}|c_i^{\mathrm{DAF}}(t)|^2-|c_i(0)|^2}\equiv\frac{1}{N}\sqrt{\sum_{i}^{N}|c_i^{\mathrm{DAF}}(t)|^2-|c_i^{\mathrm{exact}}(t)|^2}, \tag{36}$$

is also conserved to an extremely high level. These two results indicate that the numerical implications of lack of formal unitarity in the DAF propagator are fairly limited and the DAF propagator conserves probability and energy up to very high accuracy.

To further ascertain the accuracy of the propagation scheme it is also important to study the phase of the DAF-propagated wave packet and compare this to that obtained from the exact propagation result in Eq. (32). We have studied the time evolution of the quantity,

$$\frac{1}{N}\sqrt{\sum_{i}^{N}\left|c_i^{\mathrm{DAF}}(t)\exp\left[\frac{\iota E_i t}{\hbar}\right]-c_i(0)\right|^2}\equiv\frac{1}{N}\|\chi(x;t)_{\mathrm{DAF}}-\chi(x;t)_{\mathrm{exact}}\|_2, \tag{37}$$

for many different time steps. Note that the terms $\chi(x;t)_{\mathrm{DAF}}$ and $\chi(x;t)_{\mathrm{exact}}$ in Eq. (37) are the coordinate representations of the respective kets and the numerator on the right-hand side is the L^2-norm of the error vector. The quantity in Eq. (37) allows us to evaluate the instantaneous error in the propagation scheme, with respect to exact diagonalization. It also allows us to study the change in such error as a function of quantum time step. In addition, the absolute integral of the quantity in Eq. (37), that is,

$$\frac{1}{T}\int_0^T dt\frac{1}{N}\sqrt{\sum_{i}^{N}\left|c_i^{\mathrm{DAF}}(t)\exp\left[\frac{\iota E_i t}{\hbar}\right]-c_i(0)\right|^2}\equiv\frac{1}{T}\int_0^T dt\frac{1}{N}\|\chi(x;t)_{\mathrm{DAF}}-\chi(x;t)_{\mathrm{exact}}\|_2, \tag{38}$$

provides a measure of the deviation in the approximate dynamics with respect to the exact dynamics, for a given length of simulation time, T. The quantity in Eq. (38) is the average length of the vector $\{|\chi_{\mathrm{DAF}}(t)\rangle-|\chi_{\mathrm{exact}}(t)\rangle\}$ where both $|\chi_{\mathrm{DAF}}(t)\rangle$ and $|\chi_{\mathrm{exact}}(t)\rangle$ have unit magnitudes. In Table I we present our results for a range of DAF parameter values, two different Δt values and for Born–Oppenheimer as well as ADMP surfaces. Table I clearly indicates that the average length of the error vector is negligible, as compared to the length of the ket vectors representing the wave packet, for the smaller time step of 0.1 fs, but clearly grows (although is still acceptable) for the larger time step of 0.5 fs.

This leads us to an investigation of the dependence of propagation error on quantum time step. The quantity in Eq. (38) is plotted in Fig. 3(a) for a range of time steps with fixed number of simulation steps. This is done for both Born–Oppenheimer and ADMP potential surfaces. A plot proportional to Δt^3 is also shown in the same figure, which indicates that the error in propagation scales as $\approx\mathcal{O}(\Delta t^3)$ with step size. This is consistent with the truncation properties of the third-order Trotter factorization[92,127] in Eq. (9). To further elaborate on this $\mathcal{O}(\Delta t^3)$ scaling of errors due to truncation in the Trotter factorization, we provide the time evolution of errors indicated in Eq. (37) [see Fig. 3(b)] for three different time steps (0.05, 0.1, and 0.2 fs); however the vertical axis has been adjusted in the following fashion. The deviations in Eq. (37) for the 0.05 fs time step have been multiplied by a factor $(2)^3$. Similarly the deviations for 0.2 fs time step have been divided by a factor $(2)^3$. Note that these scaling factors are obtained based on the expected $\mathcal{O}(\Delta t^3)$ scaling. Clearly, the deviations after scaling are minimal over a $\sim$30 ps time scale. Thus the dominant truncation error in the quantum propagation is $\mathcal{O}(\Delta t^3)$, consistent with Trotter factorization. However, while integrating differential equations there is another kind of error that one must be aware of and these are called the global errors.[124,129,130] These errors arise when properties are calculated over a fixed total time simulation and are related to the accumulation of errors at each simulation step. Figure 3(c) presents the behavior of propagation error for a fixed total simulation time [as opposed to fixed number of steps in Fig. 3(a)]. The deviations in this error scales quadratically with step size and is consistent with a discussion of Trotter factorization, in Refs. 129 and 130, for classical propagation. Thus we conclude that the dominant source of errors in our propagation scheme is due to the order of truncation in Eq. (9).

Furthermore, the convergence of results with respect to DAF parameters is already clear from Table I. In Fig. 4 we

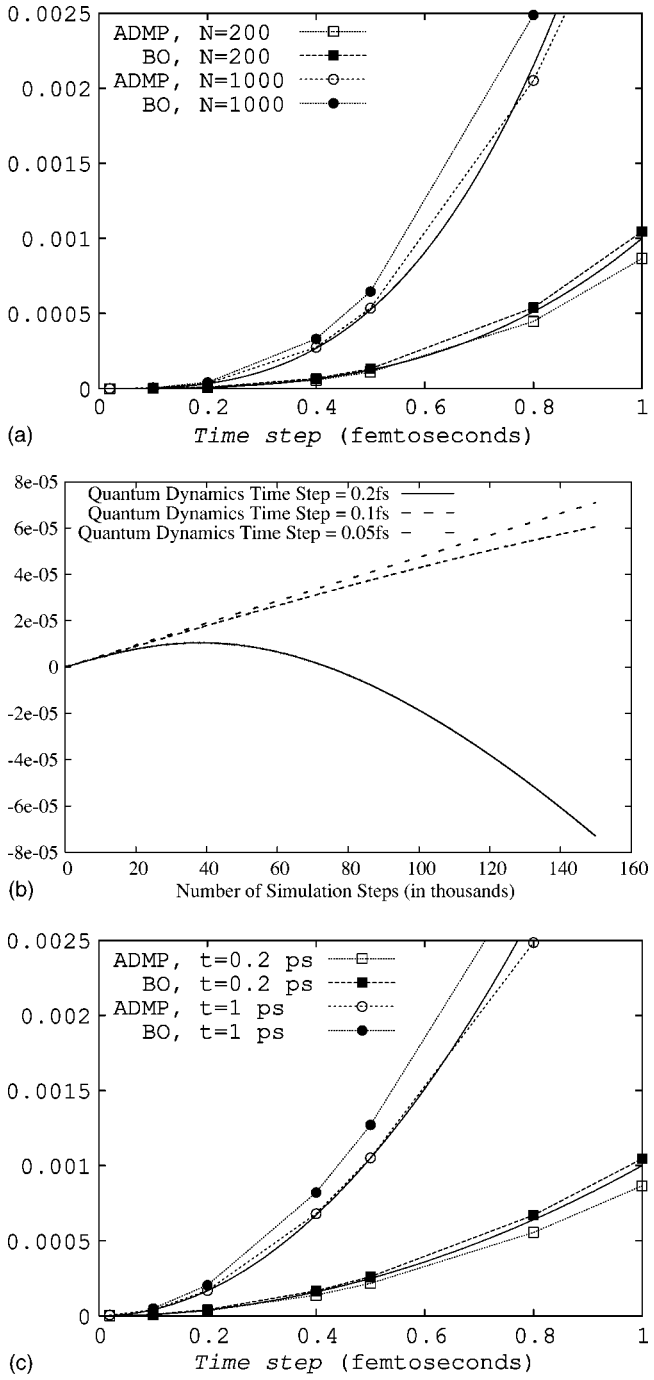

FIG. 3. (a) The $\mathcal{O}(\Delta t^3)$ scaling of errors during the quantum dynamics as calculated using Eq. (38). A plot proportional to Δt^3 is also shown for comparison. This result shows that the dominant error in our algorithm is due to Trotter factorization [see Eq. (9)]. (b) The deviations in Eq. (37) are presented for three different time steps with the vertical axis adjusted to expose the Δt^3 dependence of errors. See the text for details. (c) The accumulation of global errors during propagation and this is obtained by plotting the error in propagation with respect to fixed simulation time. As can be seen, this has a $\mathcal{O}(\Delta t^2)$ scaling and a plot of $a\Delta t^2$ is also shown for comparison. Calculations are performed using $M=60$.

study the evolution of the L^2-norm of the error vector in Eq. (37) for many different DAF parameters for both ADMP and BO calculations. The results are shown relative to the respective size of the error vector for DAF parameter $M=60$. It is clear that the size of the error vector relative to this reference is really small, which indicates that the calculations are already converged at $M=20$.

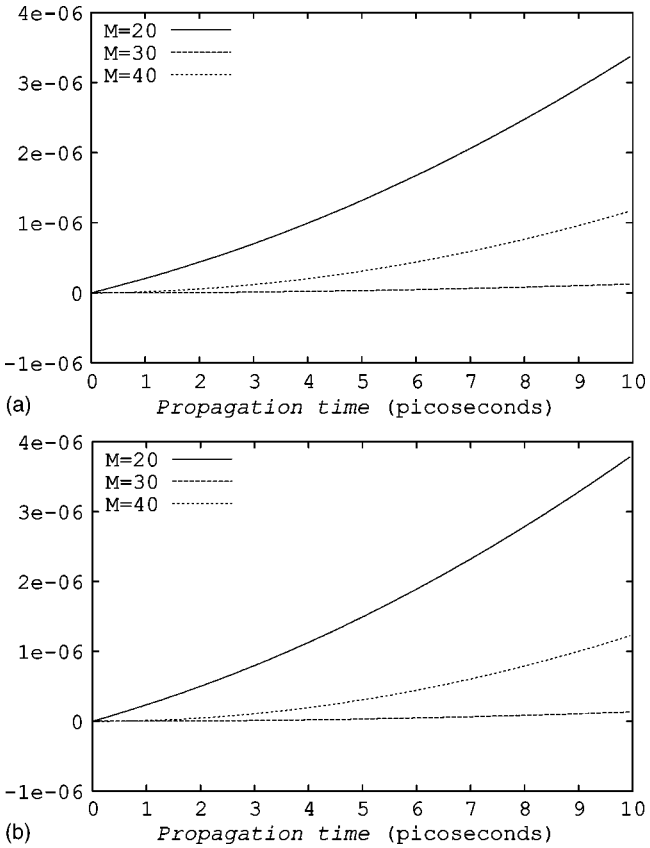

FIG. 4. The time dependence of the length of the error vector from Eq. (37) relative to that at $M=60$. (a) $\Delta t=0.1$ fs, ADMP surface, (b) $\Delta t=0.1$ fs, BO surface.

B. Comparison of results between wave packet ADMP and wave packet Born–Oppenheimer

Having shown the numerical validity of the quantum propagation, we now embark on describing the performance of the wave packet ADMP and wave packet Born-Oppenheimer schemes. The $Cl_2^{2-}H^+$ system was propagated starting from a wide range of chloride–chloride distances and initial position of the quantum proton. Unlike in the previous section, the chloride ions were allowed to move as per ADMP or Born–Oppenheimer dynamics. However, to keep the cluster stable for the full length of the simulation (that is to avoid unnecessary dissociation effects to influence the numerical tests), the motion of chloride ions was controlled by substituting larger isotope masses in all the calculations. The initial wave packet, representing the shared quantum proton, was chosen to be a simple Gaussian, as in Eq. (35), with exponent $\approx 1/(4\pi)$ Å.

Table II summarizes the comparison of ADMP and Born–Oppenheimer dynamics results for different DAF propagator parameters. The table contains data only from one starting geometry ($R_{Cl^-–Cl^-}=4.2$ Å). The results from all other simulations are in similar agreement. The calculated test parameters include the root mean square expectation values of position and momentum operators for the quantum proton, their respective uncertainties and deviations of the total energy (energy conservation) during the dynamics. These are in good agreement between the Born–Oppenheimer and ADMP simulations and the DAF polyno-

TABLE II. Comparison of wave packet Born–Oppenheimer (WP-BO) and wave packet ADMP (WP-ADMP) schemes.

Method	M	$\sigma(0)$	$\langle\hat{x}\rangle$[a]	$\langle\hat{p}\rangle$[b]	$\langle\hat{p}\rangle^2/2m$[c]	Δx[d]	Δp[e]	ΔE[f]
WP-BO	20	1.574	…	…	…	0.373	4.626	7.7
WP-ADMP	20	1.574	0.128	1.099	0.206	0.356	4.377	17.1
WP-ADMP	30	1.880	0.128	1.099	0.206	0.356	4.377	16.0
WP-ADMP	40	2.139	0.128	1.099	0.206	0.356	4.377	16.0

[a]rms deviation of the wave packet center, $\langle\chi(t)|\hat{x}|\chi(t)\rangle$, (in angstroms).
[b]rms deviation of the wave packet momentum, $\langle\chi(t)|\hat{p}|\chi(t)\rangle$, (in a.u.).
[c]In kcal/mol.
[d]rms of wave packet coordinate dispersion, $\sqrt{\langle\hat{x}^2\rangle-\langle\hat{x}\rangle^2}$ (in angstroms).
[e]rms of Wave packet momentum dispersion, $\sqrt{\langle\hat{p}^2\rangle-\langle\hat{p}\rangle^2}$ (in a.u.).
[f]rms deviation in total energy during dynamics (in microhartree).

mial size of $M=20$ seems to be large enough to describe the physical details of this problem, as already seen in Sec. III A. The deviations in the rms position expectation value are within a tenth of an angstrom while the energy penalty due to deviations in the rms momentum expectation value is approximately two-tenths of a kcal/mol. One striking feature in Table II is the fact that the product of position and momentum dispersions deviate substantially from the initial Gaussian minimal uncertainty product value. This is, of course, to be expected since the time evolution in the current method is fully quantum mechanical and there is no need for the wave packet to remain a coherent state during the dynamics process. Furthermore, the total energy conservation is in the microhartree range for both BO and ADMP forms of the approach.

In Fig. 5 the average potential energy of the system, $\langle\chi(t)|E(\{\mathbf{R_C},\mathbf{P_C}\},R_{\mathrm{QM}})|\chi(t)\rangle$, is shown for different values of the DAF parameters for ADMP and BO dynamics. The instantaneous fluctuations are generally of the order of 1 kcal/mol. In addition, the average potential energy of the sampled dynamics is in reasonable agreement between the ADMP and Born–Oppenheimer trajectories. This is important since the ADMP approach is computationally less demanding as compared to the Born–Oppenheimer approach, since the former does not require the solution to be a matrix eigenvalue problem. Based on the results presented in Table II and Fig. 5 and similar results for other starting geometries, we conclude that the path error between ADMP and Born–Oppenheimer subdynamics is small and $M=20$ is an acceptable truncation of the DAF propagator expansion given in Eq. (10).

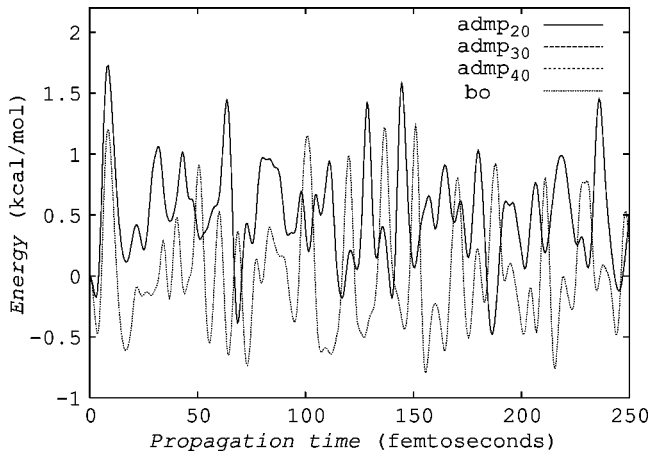

FIG. 5. Time evolution of the change in average potential energy $\langle\chi(t)|E(\{\mathbf{R_C},\mathbf{P_C}\},R_{\mathrm{QM}})|\chi(t)\rangle$ for BO and ADMP wave packet simulations of the $Cl_2^-H^+$ system. The legend admp_M indicates the value of M used in the DAF propagator while treating the chloride atoms with ADMP. The data for $M=20$, $M=30$, and $M=40$, in the ADMP wave packet simulations are not distinguishable and are seen as a single solid line. The average potential energies over the entire simulation for the ADMP trajectories are approximately 0.5 kcal/mol relative to the initial potential energy. The average potential energies over the entire simulation for the BO trajectories are approximately 0.025 kcal/mol.

C. Phenol-amine system: Scattering amplitudes from the wave packet ADMP procedure

To further illustrate the scalability of the approach with system size, we have carried out calculations on the proton transfer in phenol-trimethylamine. This system has been considered prototypical for condensed phase proton transfer.[40] In addition, similar systems have been recently studied to understand the quantum nuclear effects involved in the slow deprotonation step of weak acid-base chemistry.[68] These studies[68] have, however, used Marcus' theory[131] to obtain quantum corrections on the proton transfer process. Here we aim to demonstrate the power of the current approach in contributing significantly to such studies by treating the electronic effects accurately within hybrid DFT; in addition full quantum dynamical effects of the hopping proton are accurately treated within the wave packet formalism. As outlined previously, these quantum effects may include zero-point effects, tunneling, as well as over-barrier reflection. Our approach is capable of handling all three effects.

The chosen system, phenol-trimethylamine (see Fig. 6), can exhibit tunneling and zero-point effects and hence a quantum treatment of at least the shared proton is essential. Furthermore, delocalized electrons in the phenol ring and polarizability of the amino group require the electrons to be treated accurately. Hence this is a classic case where the loss of the proton from the phenol may be stabilized by the delocalization of electrons in the ring, depending upon the surrounding environment. The electronic structure is treated here within the level of DFT, using B3LYP and BLYP density functionals for comparison. From our study we obtain the change in scattering matrix elements (for the proton transfer) with respect to initial wave packet energy for both

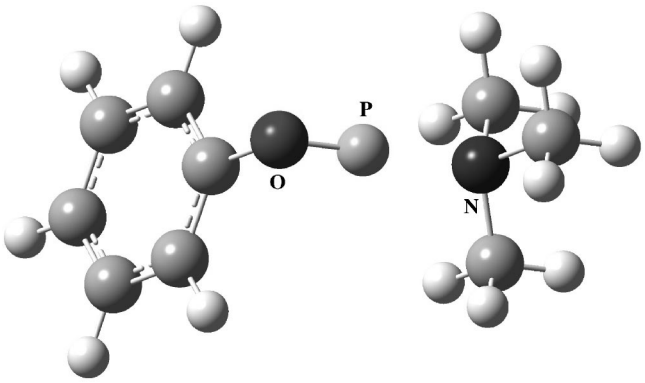

FIG. 6. The phenol-amine system. The shared proton, the oxygen of the phenol, and the nitrogen in the amine are marked. The shared proton is studied using wave packet dynamics and the rest of the system is treated using ADMP.

B3LYP and BLYP treatment of electronic degrees of freedom. This aspect is further discussed in the following. The phenol-trimethylamine system has been previously studied[40] in a methanol solvent, however, solvent molecules are excluded from the current study, to simplify the problem. Future studies will involve the treatment of a major portion of the surrounding methanol molecules using molecular mechanics along with a QM/MM implementation of the procedure illustrated here.

In Fig. 7 we present a comparison of the velocity–velocity autocorrelation function obtained from (a) classical treatment of all nuclei, and (b) quantum wave packet treatment of the shared proton. For the latter case, a wave packet centroid is extracted using $\langle\chi|\hat{x}|\chi\rangle$ and its velocity is determined via finite difference. The differences between the two correlation functions are significant. Since the wave packet does not split during the simulation time studied here (unlike the $Cl_2^{2-}H^+$ case treated in the previous sections), using the wave packet center velocity in Fig. 7 is physically meaningful. However, when this is not the case (i.e., when the quantum wave packet does split) it is necessary to analyze the full quantum wave packet instead. It must also be noted here that

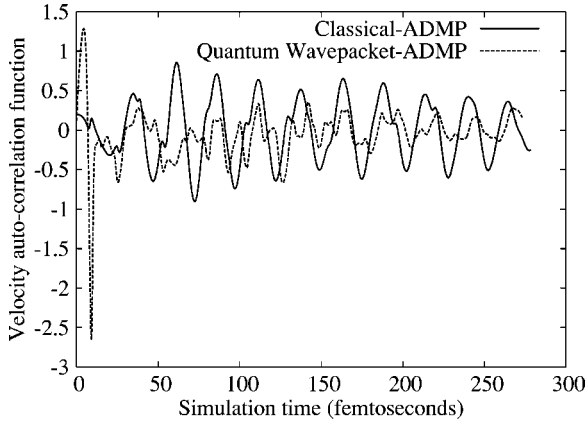

FIG. 7. Comparison of the velocity–velocity autocorrelation function for wave packet center and classical proton using BLYP/6-31+G^{**} to describe the electronic structure. The autocorrelation function for the wave packet center is obtained from finite difference. Note the high correlation exhibited by the quantum wave packet which coincides with its initial delocalization seen in Fig. 6. Similar results are also seen at the B3LYP/6-31+G^{**} level.

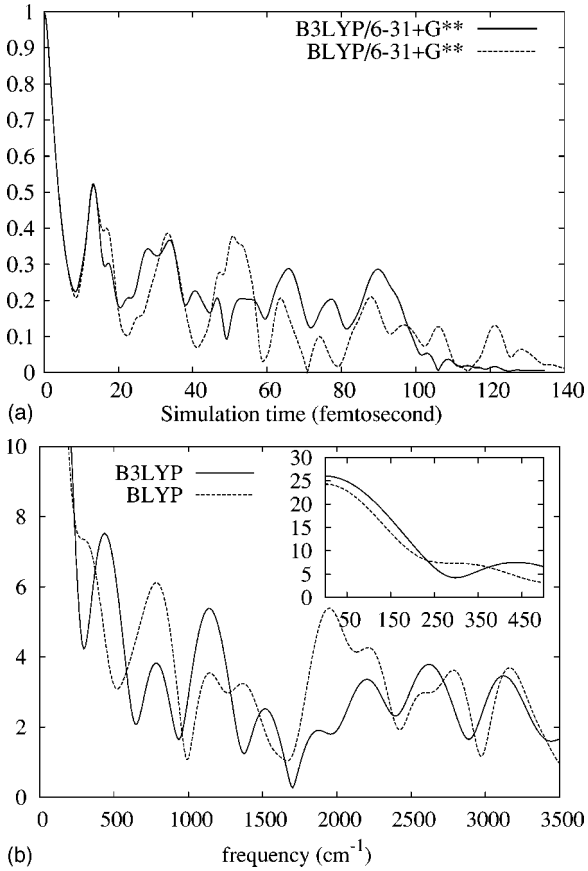

FIG. 8. The quantity $\langle\chi_0|\chi(t)\rangle$ as a function of simulation time in (a) determines the survival of the wave packet in the reactant channel. The half-Fourier transform of $\langle\chi_0|\chi(t)\rangle$ in (b) is directly proportional to the scattering matrix elements obtained from *S*-matrix Kohn variational principle (Ref. 55). The inset in (b) indicates the behavior for low scattering energies.

the full quantum nature of the propagation scheme described in Eq. (10) allows for an automatic treatment of such splitting, as seen in the previous sections.

In Fig. 8 we provide the wave packet survival time in the reactant channel, $\langle\chi_0|\chi(t)\rangle$ and its half Fourier transform:

$$\int_0^\infty dt\, \exp\{\iota Et/\hbar\}\langle\chi_0|\chi(t)\rangle \equiv \lim_{\epsilon\to 0}\left\langle \chi_0 \left| \frac{-\iota\hbar}{E-H+\iota\epsilon} \right| \chi_0 \right\rangle = \langle\chi_0|G^+(E)|\chi_0\rangle. \tag{39}$$

The operator $G^+(E)\equiv[\lim_{\epsilon\to 0}-\iota\hbar(E-H+\iota\epsilon)^{-1}]$ is the causal Green's function. It has been shown[12,54] that such a half Fourier transform is directly proportional to the scattering matrix element obtained from the *S*-matrix Kohn variational principle.[61] Figure 8 reveals marked differences between *S*-matrix element obtained from B3LYP and BLYP functionals, especially for intermediate scattering energies. For example, the *S*-matrix element at an energy of approximately 2000 cm^{-1} is three times as much for BLYP as it is for B3LYP. Important differences are also seen in the survival time in the intermediate time region. In this region of intermediate time, the proton is partially bound to both phenol and amine and in such situations B3LYP and BLYP have been previously noted[66,117] to provide significantly different

results. (See Refs. 66 and 117 where B3LYP and BLYP provide different hopping rates for proton translocation across a water wire in a Gramicidin A ion channel and in medium sized protonated water clusters.) From our treatment, we see that these differences in the intermediate time region lead directly to a discrepancy in the *S*-matrix obtained from the two functionals. Dynamical quantities such as transition probabilities and scattering matrix elements could, thus, be substantially different between the hybrid B3LYP and pure BLYP functionals when nuclear quantization is fully exploited. Thus accurate treatment of the surrounding electrons could be critical when treating proton transfer problems such as the ones discussed here. A more detailed analysis of such problems using the current methodology is one of our future goals. Importantly the current approach allows accurate treatment by employing hybrid functionals thus facilitating in-depth analysis based on such comparisons.

IV. CONCLUSION

In this contribution, we have introduced an approach to perform efficient quantum dynamics of electronic and nuclear degrees of freedom. The salient features of the method include formally exact, accurate, and efficient quantum dynamics using an analytic banded representation for the free propagator and efficient electronic dynamics using ADMP or Born–Oppenheimer dynamics. The quantum dynamics is performed using an analytic banded distributed approximating functional representation for the discretized free propagator and adaptive grids are used to render an efficient implementation of wave packet dynamics. While the quantum dynamics is currently performed using a third-order Trotter factorization, the effect of other schemes will be studied in future publications. The electronic structure is treated accurately using hybrid or gradient corrected density functionals. State of the art, higher order density functionals[88] can be easily included in the current scheme and such effects will be investigated as part of future studies.

We have tested the methodology by comparing the quantum dynamics portion of the approach with results obtained from exact diagonalization. We find the agreement to be very good. In addition we find similar agreement between the various dynamical averages obtained from treating the electronic degrees of freedom either within the ADMP formalism or within the Born–Oppenheimer formalism, in conjunction with quantum wave packet dynamics. This is particularly encouraging since ADMP has been shown to be computationally superior to Born–Oppenheimer dynamics. Hence we envision that this approach will be useful to study quantum dynamics in large systems. Future methodological improvements will allow larger and more accurate simulations. The first, critical, area where computational improvement will be necessary is in the evaluation of the potential and forces on the grid. This is an important bottleneck in the current algorithm. Multidimensional splines along with targeted potential sampling based on the local curvature and gradient are currently under development and will be used to enhance the computational strategy. Other generalizations, such as inclusion of QM/MM treatment is critical for proton transfer in large systems and this is also currently under study.

ACKNOWLEDGMENTS

This research was supported by the Camille and Henry Dreyfus Foundation and the Indiana University, Chemistry Department.

APPENDIX: COMPUTATIONAL EFFICIENCY OF WAVE PACKET ADMP OVER WAVE PACKET BORN–OPPENHEIMER DYNAMICS

In this section we present an explanation for the computational efficiency of ADMP over Born–Oppenheimer dynamics. In Born–Oppenheimer dynamics, the density matrix elements (or the molecular orbital coefficients) need to be iteratively converged at every dynamics step. Assuming that the largest possible time step is used during dynamics, this SCF convergence requires approximately 8–12 steps. (This, of course, depends on the convergence threshold and difficult systems such as transition metal complexes may require more SCF steps.) ADMP, on the contrary, is not an iterative method with respect to convergence of the density matrix and requires only one SCF step per dynamics step to calculate the Fock matrix needed for density matrix propagation [see Eqs. (22), (23), and (28)]. Both BOMD and ADMP need the nuclear gradients [Eq. (27)] which requires approximately the same amount of time in both methods.

The calculation of the nuclear force per ADMP or BO step requires approximately three times the computation time required for a single SCF CPU cycle. This makes ADMP faster than BOMD by slightly over a factor 4 per potential evaluation step (or classical ADMP/BOMD step) of the current wave packet *ab initio* dynamics approach. This step is, of course, to be repeated as many times as there are grid points to describe the quantum wave packet in the current scheme.

However, it has been noted[63] that BOMD could allow larger time steps, but to maintain similar energy conservation the BOMD time step could be at most twice as large as those in ADMP.[63] This cuts into the gain in efficiency from using ADMP by a factor of 2; the need to evaluate the potential energy and gradients at all the grid points in the current scheme is, however, expected to far exceed this loss of a factor of 2 in efficiency.

[1] *Dynamics of Molecules and Chemical Reactions*, edited by R. E. Wyatt and J. Z. H. Zhang (Dekker, New York, 1996).
[2] *Classical and Quantum Dynamics in Condensed Phase Simulations*, edited by B. J. Berne, G. Ciccotti, and D. F. Coker (World Scientific, Singapore, 1997).
[3] G. C. Schatz and A. Kupperman, J. Chem. Phys. **65**, 4642 (1976).
[4] J. B. Delos, Rev. Mod. Phys. **53**, 287 (1981).
[5] M. D. Feit and J. A. Fleck, J. Chem. Phys. **78**, 301 (1982).
[6] R. Kosloff, Annu. Rev. Phys. Chem. **45**, 145 (1994).
[7] C. Leforestier, R. H. Bisseling, C. Cerjan, M. D. Feit, R. Freisner, A. Guldberg, A. Hammerich, D. Jolicard, W. Karrlein, H. D. Meyer *et al.*, J. Comput. Phys. **94**, 59 (1991).
[8] P. DeVries, NATO ASI Ser., Ser. B **171**, 113 (1988).
[9] H. W. Jang and J. C. Light, J. Chem. Phys. **102**, 3262 (1995).
[10] S. C. Althorpe and D. C. Clary, Annu. Rev. Phys. Chem. **54**, 493 (2003).
[11] Y. Huang, S. S. Iyengar, D. J. Kouri, and D. K. Hoffman, J. Chem. Phys. **105**, 927 (1996).

[12]W. H. Miller, S. D. Schwartz, and J. W. Tromp, J. Chem. Phys. **79**, 4889 (1983).
[13]N. Makri, Comput. Phys. Commun. **63**, 389 (1991).
[14]J. Cao and G. A. Voth, J. Chem. Phys. **100**, 5093 (1994).
[15]J. Cao and G. A. Voth, J. Chem. Phys. **100**, 5106 (1994).
[16]J. Cao and G. A. Voth, J. Chem. Phys. **101**, 6168 (1994).
[17]S. Jang and G. A. Voth, J. Chem. Phys. **111**, 2357 (1999).
[18]S. Jang and G. A. Voth, J. Chem. Phys. **111**, 2371 (1999).
[19]M. D. Feit and J. A. Fleck, J. Chem. Phys. **79**, 301 (1983).
[20]M. D. Feit and J. A. Fleck, J. Chem. Phys. **80**, 2578 (1984).
[21]D. Kosloff and R. Kosloff, J. Comput. Phys. **52**, 35 (1983).
[22]D. Kosloff and R. Kosloff, J. Chem. Phys. **79**, 1823 (1983).
[23]H. Tal-Ezer and R. Kosloff, J. Chem. Phys. **81**, 3967 (1984).
[24]B. Hartke, R. Kosloff, and S. Ruhman, Chem. Phys. Lett. **158**, 223 (1986).
[25]S. S. Iyengar, D. J. Kouri, and D. K. Hoffman, Theor. Chem. Acc. **104**, 471 (2000).
[26]J. V. Lill, G. A. Parker, and J. C. Light, Chem. Phys. Lett. **89**, 483 (1982).
[27]J. C. Light, I. P. Hamilton, and J. V. Lill, J. Chem. Phys. **82**, 1400 (1985).
[28]D. T. Colbert and W. H. Miller, J. Chem. Phys. **96**, 1982 (1992).
[29]Y. Huang, D. J. Kouri, M. Arnold, I. Thomas L. Marchioro, and D. K. Hoffman, Comput. Phys. Commun. **80**, 1 (1994).
[30]I. S. Y. Wang and M. Karplus, J. Am. Chem. Soc. **95**, 8160 (1973).
[31]C. Leforestier, J. Chem. Phys. **68**, 4406 (1978).
[32]R. Car and M. Parrinello, Phys. Rev. Lett. **55**, 2471 (1985).
[33]K. Bolton, W. L. Hase, and G. H. Peslherbe, *Modern Methods for Multidimensional Dynamics Computation in Chemistry* (World Scientific, Singapore, 1998), p. 143.
[34]H. B. Schlegel, J. M. Millam, S. S. Iyengar, G. A. Voth, A. D. Daniels, G. E. Scuseria, and M. J. Frisch, J. Chem. Phys. **114**, 9758 (2001).
[35]E. Deumens, A. Diz, R. Longo, and Y. Öhrn, Rev. Mod. Phys. **66**, 917 (1994).
[36]M. D. Hack and D. G. Truhlar, J. Phys. Chem. A **104**, 7917 (2000).
[37]W. H. Miller, J. Phys. Chem. A **105**, 2942 (2001).
[38]E. J. Heller, J. Chem. Phys. **62**, 1544 (1975).
[39]G. A. Fiete and E. J. Heller, Phys. Rev. A **68**, 022112 (2003).
[40]S. Hammes-Schiffer and J. Tully, J. Chem. Phys. **101**, 4657 (1994).
[41]T. J. Martinez, M. Ben-Nun, and G. Ashkenazi, J. Chem. Phys. **104**, 2847 (1996).
[42]D. A. Micha, J. Phys. Chem. A **103**, 7562 (1999).
[43]M. C. Payne, M. P. Teter, D. C. Allan, T. A. Arias, and J. D. Joannopoulos, Rev. Mod. Phys. **64**, 1045 (1992).
[44]D. Marx and J. Hutter, *Modern Methods and Algorithms of Quantum Chemistry* (John von-Neumann Institute for Computing, Julich, 2000), Vol. 1, pp. 301–449.
[45]H. B. Schlegel, J. Comput. Chem. **24**, 1514 (2003).
[46]It should be noted that although "on-the-fly" approaches to electron-nuclear dynamics are nearly as old as quantum mechanics itself (see e.g., Refs. 69 and 84) they have generally become indispensable in recent times.
[47]D. K. Remler and P. A. Madden, Mol. Phys. **70**, 921 (1990).
[48]M. Pavese, D. R. Berard, and G. A. Voth, Chem. Phys. Lett. **300**, 93 (1999).
[49]M. E. Tuckerman and D. Marx, Phys. Rev. Lett. **86**, 4946 (2001).
[50]B. Chen, I. Ivanov, M. L. Klein, and M. Parrinello, Phys. Rev. Lett. **91**, 215503 (2003).
[51]S. S. Iyengar, H. B. Schlegel, J. M. Millam, G. A. Voth, G. E. Scuseria, and M. J. Frisch, J. Chem. Phys. **115**, 10291 (2001).
[52]The (i,j)th element of a Toeplitz matrix depends only on $|i-j|$. This property of the free propagator used in the current contribution yields an efficient scheme where only the first (banded) row of the matrix representation of the time-evolution operator needs to be stored.
[53]D. K. Hoffman, N. Nayar, O. A. Sharafeddin, and D. J. Kouri, J. Phys. Chem. **95**, 8299 (1991).
[54]D. K. Hoffman and D. J. Kouri, J. Phys. Chem. **96**, 9631 (1992).
[55]D. J. Kouri, Y. Huang, and D. K. Hoffman, Phys. Rev. Lett. **75**, 49 (1995).
[56]T. L. Marchioro II, M. Arnold, D. K. Hoffman, W. Zhu, Y. H. Huang, and D. J. Kouri, Phys. Rev. E **50**, 2320, (1994).
[57]D. K. Hoffman, M. Arnold, and D. J. Kouri, J. Phys. Chem. **96**, 6539 (1992).
[58]S. Goedecker, Rev. Mod. Phys. **71**, 1085 (1999).
[59]G. E. Scuseria, J. Phys. Chem. A **103**, 4782 (1999).
[60]C. A. White and M. Head-Gordon, J. Chem. Phys. **101**, 6593 (1994).
[61]R. G. Newton, *Scattering Theory of Waves and Particles* (Springer, New York, 1982).
[62]S. S. Iyengar, D. J. Kouri, and D. K. Hoffman, Theor. Chem. Acc. **104**, 471 (2000).
[63]H. B. Schlegel, S. S. Iyengar, X. Li, J. M. Millam, G. A. Voth, G. E. Scuseria, and M. J. Frisch, J. Chem. Phys. **117**, 8694 (2002).
[64]S. S. Iyengar, H. B. Schlegel, G. A. Voth, J. M. Millam, G. E. Scuseria, and M. J. Frisch, Isr. J. Chem. **42**, 191 (2002).
[65]S. S. Iyengar, H. B. Schlegel, and G. A. Voth, J. Phys. Chem. A **107**, 7269 (2003).
[66]N. Rega, S. S. Iyengar, G. A. Voth, H. B. Schlegel, T. Vreven, and M. J. Frisch, J. Phys. Chem. B **108**, 4210 (2004).
[67]S. S. Iyengar and M. J. Frisch, J. Chem. Phys. **121**, 5061 (2004).
[68]C. Costentin and J.-M. Saveant, J. Am. Chem. Soc. **126**, 14787 (2004).
[69]P. A. M. Dirac, *The Principles of Quantum Mechanics*, The International series of monographs on Physics vol. 27, 4th ed. (Oxford University Press, New York, 1958).
[70]R. B. Gerber, V. Buch, and M. A. Ratner, J. Chem. Phys. **77**, 3022 (1982).
[71]R. H. Bisseling, R. Kosloff, R. B. Gerber, M. A. Ratner, L. Gibson, and C. Cerjan, J. Chem. Phys. **87**, 2760 (1987).
[72]J. C. Tully, Faraday Discuss. **110**, 407 (1998).
[73]J. J. Sakurai, *Modern Quantum Mechanics* (Addison–Wesley, Reading, MA, 1994).
[74]E. Madelung, Z. Phys. **40**, 322 (1926).
[75]L. de Broglie, *An Introduction to the Study of Wave Mechanics* (Dutton, Inc., New York, 1930).
[76]L. de Broglie, Compt. Rend. **183**, 447 (1926).
[77]L. de Broglie, Compt. Rend. **184**, 273 (1927).
[78]L. de Broglie, Compt. Rend. **185**, 380 (1927).
[79]D. Bohm, Phys. Rev. **85**, 166 (1952).
[80]*Bohmian Mechanics: An Appraisal*, edited by J. T. Cushing, A. Fine, and S. Goldstein (Kluwer, Boston, 1996).
[81]P. R. Holland, *The Quantum Theory of Motion* (Cambridge, University Press New York, 1993).
[82]H. C. Andersen, J. Chem. Phys. **72**, 2384 (1980).
[83]M. Parrinello and A. Rahman, Phys. Rev. Lett. **45**, 1196 (1980).
[84]J. Frenkel, *Wave Mechanics* (Oxford University Press, Oxford, 1934).
[85]A. D. Becke, J. Chem. Phys. **98**, 5648 (1993).
[86]A. D. Becke, J. Chem. Phys. **38**, 3098 (1988).
[87]J. P. Perdew, K. Burke, and M. Ernzerhof, Phys. Rev. Lett. **77**, 3865 (1996).
[88]J. Tao, J. P. Perdew, V. N. Staroverov, and G. E. Scuseria, Phys. Rev. Lett. **91**, 146401 (2003).
[89]R. McWeeny, Rev. Mod. Phys. **32**, 335 (1960).
[90]See Ref. 65 for a detailed exposition on the similarities between the basis sets used in ADMP and the wavelet theory (Refs. 105–108) of multiresolution analysis.
[91]G. H. Golub and C. F. van Loan, *Matrix Computations* (The Johns Hopkins University Press, Baltimore, 1996).
[92]M. F. Trotter, Proc. Am. Math. Soc. **10**, 545 (1959).
[93]D. Neuhauser, J. Chem. Phys. **95**, 4927 (1991).
[94]G. Arfken, *Mathematical Methods for Physicists* (Academic, New York, 1985).
[95]R. C. Mowrey and D. J. Kouri, J. Chem. Phys. **84**, 6466 (1986).
[96]R. P. Feynman and A. R. Hibbs, *Quantum Mechanics and Path Integrals* (McGraw-Hill, New York, 1965).
[97]L. S. Schulman, *Techniques and Applications of Path Integration* (Wiley, New York, 1986).
[98]D. Chandler and P. G. Wolynes, J. Chem. Phys. **74**, 4078 (1981).
[99]B. J. Berne and D. Thirumalai, Annu. Rev. Phys. Chem. **37**, 401 (1986).
[100]D. K. Hoffman, T. L. Marchioro, M. Arnold, Y. H. Huang, W. Zhu, and D. J. Kouri, J. Math. Chem. **20**, 117 (1996).
[101]D. K. Hoffman, G. W. Wei, D. S. Zhang, and D. J. Kouri, Phys. Rev. E **57**, 6152 (1998).
[102]D. K. Hoffman, G. W. Wei, and D. J. Kouri, J. Math. Chem. **25**, 235 (1999).
[103]S. S. Iyengar, G. A. Parker, D. J. Kouri, and D. K. Hoffman, J. Chem. Phys. **110**, 10283 (1999).
[104]X. Li and S. S. Iyengar (unpublished).
[105]A. Grossman and J. Morlet, SIAM J. Math. Anal. **15**, 723 (1984).
[106]G. Strang, SIAM Rev. **31**, 613 (1989).
[107]I. Daubechies, *Ten Lectures in Wavelets* (SIAM, Philadelphia, PA, 1992).
[108]G. Strang and T. Nguyen, *Wavelets and Filter Banks* (Wellesley-Cambridge Press, Cambridge, 1996).
[109]For exceptions please see Refs. 101 and 102.

[110] J. R. Klauder and B.-S. Skagerstam, *Coherent States: Applications in Physics and Mathematical Physics* (World Scientific, Singapore, 1985).
[111] J. R. Klauder and I. Daubechies, Phys. Rev. Lett. **52**, 1161 (1984).
[112] Y. Zhao, S. Yokojima, and G. Chen, J. Chem. Phys. **113**, 4016 (2000).
[113] J. Morales, E. Deumens, and Y. Ohrn, J. Math. Phys. **40**, 766 (1999).
[114] P. Pulay, Mol. Phys. **17**, 197 (1969).
[115] F. Riesz and B. Sz.-Nagy, *Functional Analysis* (Dover, New York, 1990).
[116] S. S. Iyengar, M. K. Petersen, T. J. F. Day, C. J. Burnham, and G. A. Voth (unpublished).
[117] S. S. Iyengar, T. J. F. Day, and G. A. Voth, Int. J. Mass. Spectrom. (in press).
[118] M. K. Petersen, S. S. Iyengar, T. J. F. Day, and G. A. Voth, J. Phys. Chem. B **108**, 14804 (2004).
[119] D. J. Kouri and D. K. Hoffman, Phys. Rev. Lett. **85**, 5263 (2000).
[120] C. Chandler and A. Gibson, J. Approx. Theory **100**, 233 (1999).
[121] S. S. Iyengar, Ph.D. thesis, University of Houston, 1998.
[122] J. Jakowski and S. S. Iyengar (unpublished).
[123] V. Fack and G. V. Berghe, J. Phys. A **20**, 4153 (1987).
[124] C. M. Bender and S. A. Orzag, *Advanced Mathematical Methods for Scientists and Engineers* (McGraw-Hill, New York, 1978).
[125] C. Alhambra, J. Corchado, M. L. Sanchez, M. Garcia-Viloca, J. Gao, and D. G. Truhlar, J. Phys. Chem. B **105**, 11326 (2001).
[126] S. Hammes-Schiffer, J. Chem. Phys. **105**, 2236 (1996).
[127] M. E. Tuckerman, B. J. Berne, and A. Rossi, J. Chem. Phys. **94**, 1465 (1991).
[128] D. J. Kouri, W. Zhu, X. Ma, B. M. Pettitt, and D. K. Hoffman, J. Phys. Chem. **96**, 9622 (1992).
[129] A. K. Mazur, J. Comput. Phys. **136**, 354 (1997).
[130] M. P. Allen and D. J. Tildesley, *Computer Simulation of Liquids* (Oxford Science, New York, 1987).
[131] R. A. Marcus, Rev. Mod. Phys. **65**, 599 (1993).